

Detection of photon-level signals embedded in sunlight with an atomic photodetector

Laura Zarraoa,¹ Romain Veyron,¹ Tomas Lamich,¹ Sondas Elsehimy,¹ and Morgan W. Mitchell^{1,2}

¹ICFO - Institut de Ciències Fotoniques, The Barcelona Institute of Science and Technology, 08860 Castelldefels, Barcelona, Spain

²ICREA - Institució Catalana de Recerca i Estudis Avançats, 08010 Barcelona, Spain

(*Electronic mail: laura.zarraoa@icfo.eu, morgan.mitchell@icfo.eu)

(Dated: 3 December 2025)

The detection of few-photon signals in a broadband background is an extreme challenge for photon counting, requiring filtering that accepts a narrow range of optical frequencies while strongly rejecting all others. Recent work [Zarraoa et. al, Phys. Rev. Res. 6, 033338 (2024)] demonstrated that trapped single atoms can act as low dark-count narrow-band photodetectors. Here we show that this “quantum jump photodetector” (QJPD) approach can also detect photon-level signals embedded in strong sunlight. Using a single rubidium atom as a QJPD, we count arrivals of individual narrow-band laser photons embedded in sunlight powers of order 10^{10} photons/s. We derive a rate-equation model for the atom’s internal-state dynamics in sunlight, and find quantitative agreement with experiment. Using this model, we calculate the channel capacity over a noisy communication channel when sending weak coherent states and detecting them in the presence of sunlight, achieving a representative rate of 0.5 bits per symbol when sending 150 probe photons per 10 ms time-bin, embedded in 1 nW of sunlight (of order 10^{10} photons/s in the visible and near-infrared bands). The demonstration may benefit background-limited applications such as daytime light detection and ranging (LIDAR), remote magnetometry, and free-space classical and quantum optical communications.

I. INTRODUCTION

Detecting weak optical signals embedded in a broadband background such as scattered sunlight is a challenge for many applications. Examples include daylight optical communications^{1–3}, daytime photon counting light detection and ranging (LIDAR)⁴ and daytime adaptive optics using laser guide stars⁵. Some strategies to deal with a high background level include the use of single-mode fibers for spatial filtering⁶, frequency filtering^{7,8}, and statistical analysis⁹. Frequency rejection of a broadband background requires filters with very broad blocking ranges, and with narrow transmission windows around the signal’s frequency. Atoms, due to their strong frequency selectivity, are a natural candidate to build such filters, and have already proven useful as a means of background filtering to increase the signal-to-noise ratios during daytime operation^{10,11}. Despite advances in background rejection, most space optical communications are still performed during the night to reduce sunlight background. The same happens in other applications such as remote magnetometry using mesospheric sodium^{12–15}, currently only performed at night, that would benefit from a detector immune to this background. Daylight operation would provide continuous observation of Earth’s magnetic field and shed light on how it interacts with space weather¹⁶.

In atmospheric sodium magnetometry, the sunlight background not only affects the detectors but also has an effect on the sodium atoms themselves: it can depolarize the atomic ensemble and lead to decoherence of the spin precession. Besides magnetometry, there is a growing number of applications where understanding the interaction of blackbody radiation (BBR) with matter is becoming important. For instance, room-temperature BBR contributes to frequency shifts in atomic clocks^{17,18}, limits the lifetime of Rydberg states^{19–21} and the states of molecules²² due to BBR absorption and

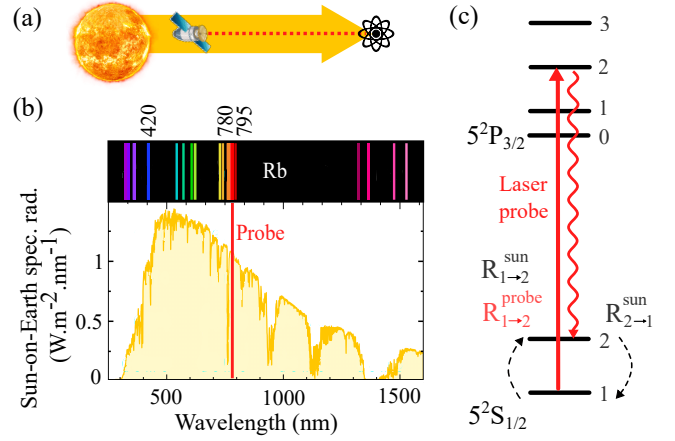


FIG. 1. (a) Visual schematic of potential applied scenario: single-photon signals from a satellite are detected using an atomic detector (a single ^{87}Rb atom) on top of a strong broadband background, e.g., sunlight. (b) Emission lines of ^{87}Rb with ground-state-connected transitions at 420 nm, 780 nm and 795 nm (top) and sunlight spectrum after passing Earth’s atmosphere (bottom). Red solid line marks the probe frequency at 780 nm. (c) Energy levels of ^{87}Rb with the relevant probe- and sun-driven transition rates.

stimulated emission, generates attractive forces on atoms^{23,24} and is a source of decoherence of matter waves in heated enclosures²⁵. Fewer works^{26,27} have studied the interaction of high-temperature BBR, such as sunlight, with atoms. In this case, the BBR spectrum is distributed around optical frequencies and therefore can directly drive atomic transitions, in contrast to the low BBR temperature which contributes mainly to atomic frequency shifts.

In this work, our results are twofold. We provide a quantitative model of sunlight-atom interaction that describes the atom’s internal dynamics, and we demonstrate experimentally

that a single-atom “quantum jump photodetector” (QJPD)²⁸ can detect single-photon signals embedded in sunlight. The paper is organized as follows. Section II presents the single-atom setup used as a QJPD and describes quantitatively the coupling of sunlight to the atom in the laboratory. Section III provides a model for describing the atom’s internal dynamics under both sunlight and weak laser probe illumination. Section IV presents experimental results using the QJPD for the detection of signal photons embedded in sunlight, with both initially coupled to a common spatial mode. Its background rejection capabilities are quantified calculating the channel capacity, i.e., the rate at which information can be transmitted over a noisy communication channel.

II. EXPERIMENTAL SETUP

In a previous work²⁸, we demonstrated a single-atom QJPD for the detection of weak coherent light and quantified its characteristics, including quantum efficiency and dark counts. Our QJPD consists of a single ^{87}Rb atom trapped by a far-off-resonance trap (FORT) surrounded by four high-NA lenses^{28–30}. It measures photons by detecting quantum jumps - changes between atomic states with different fluorescence behavior, in our case between the $F = 1$ and $F = 2$ hyperfine levels of the $\text{Rb } 5^2\text{S}_{1/2}$ ground state (hereafter $|1\rangle$, and $|2\rangle$, respectively) - caused by photon absorptions (Figure 1c).

The experimental system is shown schematically in Figure 2. The atom is loaded into the FORT, with trap depth $790\text{ }\mu\text{K}$, cooled by polarization gradient cooling down to $20\text{ }\mu\text{K}$ and then optically pumped to $|1\rangle$ by a 27 ms duration pulse tuned $3\Gamma_0$ to the red of the $F = 2 \rightarrow F' = 3$ transition, where $\Gamma_0 = 2\pi \times 6.065\text{ MHz}$ is the transition linewidth. It is then exposed to sunlight and probed for a duration of $t_{\text{exp}} = 10\text{ ms}$. Sunlight can excite the atom via both the D_1 and D_2 transitions, whereas the probe is tuned to resonance with the $F = 1 \rightarrow F' = 2$ transition of the D_2 line, as seen in Figure 1c. The atomic state is then read out for 1 ms by hyperfine-state selective fluorescence detection. For the experiments presented here, the measured quantum jump efficiency for single photon absorption is $\eta_{\text{QJ}} = 8.5(5) \times 10^{-3}$, a factor of two higher than previous work²⁸ due to better atom localization in the trap.

Sunlight is coupled into a single-mode fiber (SMF) using a collimator (Schäfter + Kirchhoff GmbH 60FC-4-A6.2s-02) mounted on a tracking LX200-ACF Meade telescope. The light is brought to the lab via concatenated single-mode fibers (Thorlabs 780HP) of lengths 35 m and 25 m , with a total transmission at 780 nm of 55% . The Sun power coupled into the SMF is monitored with a power meter (Thorlabs S151C) that integrates the power over the entire spectrum with a wavelength-dependent responsivity. The total irradiance of the Sun, integrated over the whole spectrum, at a distance of one astronomical unit is known as the solar constant³¹, and its average value is 1.361 kW/m^2 . Around 20% to 30% of this is lost in the atmosphere³², leading to the typical value of total solar irradiance at Earth’s surface of 1 kW/m^2 . From that, there are roughly 10 mW of Sun power arriving to the colli-

mator, given it has an input area of $\approx 10^{-5}\text{ m}^2$. Of those, on bright days, the maximum total power coupled into the fiber was around $6\text{ }\mu\text{W}$ at the telescope and around $3\text{ }\mu\text{W}$ at the lab. Such low collection efficiency is expected due to the multi-spatial-mode character of sunlight, of which only one mode can be carried by the fiber²⁶. We note that even for starlight, which has much greater spatial coherence, the efficiency of coupling into SMF can be low, e.g., 0.45% in Sliski et al.³³.

Here, we directly measured the spectral radiance in the lab before focusing (right axis on Figure 2c) from which we will later compute the transition rates at the atom position. The integrated maximum Sun power after the optics, deconvolved from the detector responsivity, is $1.38\text{ }\mu\text{W}$, which corresponds to 51.2 fW at 780 nm within the 6 MHz atom linewidth.

Sunlight and probe are combined and monitored using two fiber 50:50 beamsplitters (BSs, Thorlabs PN780R5A2). The “probe BS” splits the probe between monitoring in single-photon avalanche detectors (SPADs) and the “Sun BS” where it is combined with sunlight. The “Sun BS” splits the combined light between monitoring and the atom chamber. The power of the probe light was controlled by an acousto-optic modulator before reaching the beamsplitters. Different sunlight powers are obtained by combinations of three absorptive neutral density (ND) filters (two NE10A and one NE05A, Thorlabs) placed before the Sun-coupling collimator. The combined light was time-gated with a free-space shutter and focused on the atom using one of the high-NA lenses.

III. MODEL FOR AN ATOM INTERACTING WITH A WEAK LASER PROBE AND SUNLIGHT

In this section, we use rate equations to describe the atom’s internal dynamics driven by resonant photons from the probe and sunlight that we later compare to the experimental results. We also provide a quantitative analysis of the effect of off-resonant photons by calculating AC Stark shifts due to sunlight.

A. Rate equation with laser probe and sunlight

Sunlight contributes to driving the atomic transitions over a broad spectrum. This results in net transition rates between $|1\rangle$ and $|2\rangle$ as shown in Figure 1. The population N_2 of the $|2\rangle$ state evolves under the influence of incoherent light or a weak coherent laser driving in $|2\rangle$ as described by the rate equation

$$\frac{dN_2}{dt} = R_{1 \rightarrow 2}N_1 - R_{2 \rightarrow 1}N_2. \quad (1)$$

If the atom starts in the state $|1\rangle$, the time evolution of the population N_2 is

$$N_2(t) = \frac{R_{1 \rightarrow 2}}{R_{1 \rightarrow 2} + R_{2 \rightarrow 1}} \left(1 - e^{-(R_{1 \rightarrow 2} + R_{2 \rightarrow 1})t} \right). \quad (2)$$

The transition rates $R_{i \rightarrow j}$ under incoherent sunlight excitation are calculated using the absorption rates given by the

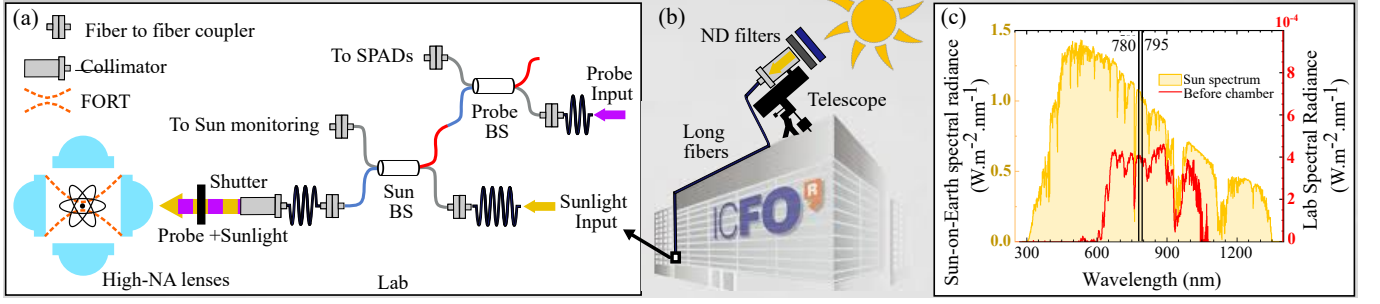


FIG. 2. Experimental setup and sunlight spectrum. (a) Sunlight and probe are combined using two fiber beam-splitters (BSs) before being sent to the atom. (b) Sunlight is collected into a single-mode fiber using a collimator mounted on the tracking base of a telescope situated on the roof of the building and sent to the lab via long fibers. (c) Comparison between the spectral radiance of sunlight past the Earth's atmosphere (yellow shaded curve) and the one measured in the lab before the chamber, shown in red. Two black vertical lines at wavelengths 780 nm and 795 nm are included for visual reference.

Einstein coefficients^{20,26}. Neglecting stimulated emission, the total rate $R_{F_i \rightarrow F_f}$ from F_i to F_f is given by an absorption from the initial state $|J_g, F_i\rangle$ towards any excited state $|e\rangle = |J_e, F_e\rangle$ with oscillator strength f_{F_i, F_e} , followed by spontaneous emission at a rate $\Gamma_{J_e J_g}$ towards the final state $|J_g, F_f\rangle$ with oscillator strength f_{F_e, F_f}

$$R_{F_i \rightarrow F_f}^{\text{sun}} = \sum_{\{e\}} \frac{\pi^2 c^3}{\hbar \omega_{J_g J_e}^3} \rho(\omega_{J_g J_e}) \Gamma_{J_e J_g} f_{F_i, F_e} f_{F_e, F_f}, \quad (3)$$

where c is the speed of light in vacuum, \hbar is the reduced Planck constant, $\omega_{J_g J_e}$ is the transition angular atomic frequency between the states J_g and J_e , and $\rho(\omega)$ is the spectral energy density for blackbody radiation defined by Planck's law (energy per volume per angular frequency)

$$\rho(\omega) = \frac{\hbar}{\pi^2 c^3} \frac{\omega^3}{e^{\hbar \omega / k_b T} - 1}. \quad (4)$$

The incident spectral energy density on Earth from the Sun is given by Eq. (4) multiplied by the solid angle subtended by the Sun as seen from Earth, times the frequency-dependent transmission through the atmosphere. The energy density can be more conveniently expressed in terms of the spectral radiance $B(\lambda) = 2\pi \nu^2 \rho(\omega)$ (power per area per wavelength) which is shown for reference in Figure 1c and has value around the Rb D lines of $B_{\text{Earth}}(\lambda_{780}) \approx 1 \text{ W m}^{-2} \text{ nm}^{-1}$.

In our setup, the part of the Sun spectrum before focusing ranges from 600 nm to 1100 nm (see Figure 2c). The transitions $5S_{1/2} \rightarrow 6P_{1/2}$ at 421 nm and $5S_{1/2} \rightarrow 6P_{3/2}$ at 420 nm, which are present in the Sun radiation, are not transmitted through the fiber and therefore do not contribute to the dynamics. The main transitions that can resonantly interact with Rb atoms are the D₁-line at 795 nm and the D₂-line at 780 nm, which overlap with the sunlight spectrum and for which $\rho(\omega_{D_1}) \approx \rho(\omega_{D_2})$. In addition, the ratios $\Gamma_{J_e J_g} / \omega_{J_g J_e}^3$ in Eq. (3) are equal for the D₁- and D₂-lines for Rb, which is therefore factorized as a single factor Γ_0 / ω_0^3 simplifying the sunlight rates to

$$R_{F_i \rightarrow F_f}^{\text{sun}} = R_0 \sum_{\{e\}} f_{F_i, F_e} f_{F_e, F_f}. \quad (5)$$

The scaling rate in Eq. (5) is $R_0 = (\pi^2 c^3 / \hbar \omega_0^3) \rho_0$ with $\rho_0 = \rho_{\text{at}}(\omega_0) \Gamma_0$ being the energy density integrated over the atomic linewidth at the angular atomic frequency $\omega_0 = 2\pi c / \lambda_0$. It directly links to the Sun intensity at ω_0 as $\rho_0 = I_{\text{at}}(\omega_0) / c$, and thus to the power $P_{\text{sun}}(\omega_0)$ for a Gaussian beam intensity by $\rho_0 = 2P_{\text{sun}}(\omega_0) / \pi w_{\text{at}}^2 c$ where w_{at} is the beam waist at the atom position. Finally, $P(\omega_0)$, the solar power within the line at ω_0 , is related to the total power P_{sun} as $P_{\text{sun}}(\omega_0) = \kappa P_{\text{sun}}$, where κ is defined in terms of the known solar spectral radiance: $\kappa \equiv B_{\text{exp}}(\lambda_0) \Delta \lambda / \int_0^\infty B_{\text{exp}}(\lambda) d\lambda$ and $\Delta \lambda$ is the transition linewidth in wavelength. The rate R_0 can therefore be expressed linearly with the total Sun power

$$R_0 = \frac{2\pi c^2}{\hbar \omega_0^3 w_{\text{at}}^2} \kappa P_{\text{sun}}. \quad (6)$$

The probe can be included in the model using an additional rate as it only drives weakly the atom. Sending on average \bar{n}_{ph} atom-resonant probe photons during the time t with a quantum jump efficiency η_{QJ} between the states $|1\rangle$ and $|2\rangle$ defines the absorption rate

$$R_{1 \rightarrow 2}^{\text{probe}} \equiv \frac{\eta_{\text{QJ}} \bar{n}_{\text{ph}}}{t}. \quad (7)$$

The theoretical efficiency η_{QJ} depends on the coupling strength of the atomic transition and the localization strength given by the numerical aperture used to focalize the photons³⁴. It also depends on the spatiotemporal overlap of the incoming photon with the atom radiation pattern. This efficiency can be precisely calibrated experimentally, incorporating in a single factor these effects²⁸. The total transition rates in Eq. (2) with both Sun and probe photons are then $R_{1 \rightarrow 2} = R_{1 \rightarrow 2}^{\text{sun}} + R_{1 \rightarrow 2}^{\text{probe}}$ and $R_{2 \rightarrow 1} = R_{2 \rightarrow 1}^{\text{sun}}$.

The spectral radiance at the atom position $B_{\text{at}}(\lambda_{780})$ is increased compared to the one at the fiber output $B(\lambda_{780})$ by the focalization of sunlight in a waist $w_{\text{at}} = 1.3 \mu\text{m}$ by an aspherical lens of focal length $f_L = 8 \text{ mm}$. For a Gaussian beam, they relate through the ratio of the beam waists as $B_{\text{at}}(\lambda_{780}) = (w_{\text{in}} / w_{\text{at}})^2 B(\lambda_{780})$, where the waist at the lens input is $w_{\text{in}} = \lambda_{780} f_L / (\pi w_{\text{at}})$.

For the maximum spectral radiance at the fiber output $B(\lambda_{780}) = 4 \times 10^{-4} \text{ W m}^{-2} \text{ nm}^{-1}$ corresponding to $P_{\text{sun}} =$

$1.38\mu\text{W}$, we get $B_{\text{at}}(\lambda_{780}) = 550\text{Wm}^{-2}\text{nm}^{-1}$ and a rate $R_0 = 2.6 \times 10^4\text{s}^{-1}$. In a typical experimental time window of 10 ms, this corresponds to about 260 scattering events.

B. AC Stark shifts induced by sunlight

So far we only considered the influence of the resonant Sun photons on the internal dynamics. However, as the light is tightly focused, we should evaluate the effect of the off-resonant photons that could lead to light shifts. The situation is different from atomic clocks where most of the room-temperature BBR is off-resonant with the relevant atomic transition, which enables calculating the light shift with an average static field plus small dynamic corrections^{17,20,35}. For sunlight, the spectrum overlaps with the Rb lines, leading to light shifts of opposite sign. To evaluate the sunlight-induced light shift, we use the full calculations of the light shift using the dynamical polarizabilities³⁶. We compute the total shift by summing the contributions at any angular frequency ω for a blackbody distribution at the Sun temperature $T = 5800\text{K}$ for a given frequency-dependent atomic polarizability $\alpha(F, \omega)$ for an atom in a hyperfine state F^{20}

$$\delta E_F = -\frac{1}{4\epsilon_0} \int_0^\infty \alpha(F, \omega) \rho(\omega) d\omega. \quad (8)$$

The energy density $\rho(\omega)$ is scaled such that the total power sent to the atom is equal to P_{sun} in a waist of $1.3\mu\text{m}$. This includes all losses, from sunlight collection to transmission losses towards the atom. Considering linearly polarized sunlight to calculate the polarizability, and performing the integration of Eq. (8) gives $\delta E_{5S_{1/2}, |1\rangle} / P_{\text{sun}} \approx -2\pi\hbar \times 30\text{Hz}/\mu\text{W}$. The excited state presents Zeeman-dependent shifts, with a maximum shift $\delta E_{5P_{3/2}, |2\rangle} / P_{\text{sun}} \approx 2\pi\hbar \times 285\text{Hz}/\mu\text{W}$ for $m_F = 0$. This leads to a maximum differential light shift on the probe transition of $2\pi\hbar \times 315\text{Hz}/\mu\text{W}$. For the Sun powers used in this work, this shift is small compared to the trap depth and atomic linewidth. This comes from the fact that the Rb lines are near the center of the Sun spectrum, experiencing light shifts that globally cancel. For instance, keeping only the wavelengths larger than 800 nm in the BBR leads to $\delta E_{5S_{1/2}, |1\rangle, \lambda > 800\text{nm}} / P_{\text{sun}} \approx -2\pi\hbar \times 530\text{Hz}/\mu\text{W}$ which is indeed higher than for the full BBR spectrum. Nevertheless, the previous numbers are an over-estimation of the expected shift. In practice, the off-resonant photons will also experience a chromatic focal shift due to the aspherical lens used to focus the light, leading to a frequency-dependent reduction of the intensity at the atom that is expected to reduce the light shifts. Note that considering an isotropic polarization for sunlight only changes slightly the results. In that case, the polarizability is scalar as the vector and tensor part average to zero. The maximum differential light shift is $2\pi\hbar \times 220\text{Hz}/\mu\text{W}$, with small variations with the Zeeman states. As a result, for rubidium atoms, the main contribution of sunlight is therefore driving the atomic transitions with resonant photons.

IV. EXPERIMENTAL RESULTS

In this section, we describe the detection of signal photons embedded in sunlight, compare it to the presented model and consider a realistic scenario for a communication link between a satellite and the detector. Finally, using these results, we calculate the channel capacity of a communication channel using such a photodetector.

A. Coupling of sunlight to a single atom

The preparation-exposure-readout sequence described in Section II is repeated 200 times for each combination of sunlight and probe photons to extract the probability and uncertainty of the atom being in $|2\rangle$ after the exposure time. Figure 3 shows experimental data of the runs when only sunlight (black rectangles) is sent to the atom during the exposure time. Experimentally, the Sun power is monitored by measuring the total power sent to the atom P_{sun} . In this case, the population of $|2\rangle$ after exposure with sunlight for a given time, $N_2^{\text{background}}(t)$, can be fitted with Eq. (2) with two free parameters

$$N_2^{\text{background}}(t) = N_2^{\text{sat,exp}} (1 - e^{-b_{\text{exp}} P_{\text{sun}} t}). \quad (9)$$

The fitted saturated population of $|2\rangle$ is $N_2^{\text{sat,exp}} = 0.66(3)$. The rate to reach this saturation under Sun illumination is found to be $b_{\text{exp}} = 9(2)\text{s}^{-1}\text{nW}^{-1}$.

By summing over all excited states in Eq. (5), we get the predicted transition rates between the two hyperfine ground states $R_{1 \rightarrow 2}^{\text{sun}} = (10/9)R_0$ and $R_{2 \rightarrow 1}^{\text{sun}} = (2/3)R_0$. This leads to a saturated population equal to $N_2^{\text{sat,th}} = (5/8) = 0.625$, consistent with the experimental result. The value $5/8$ reflects the fact that the Sun is driving multiple transitions between hyperfine states with slightly different total transfer rates between $|1\rangle$ and $|2\rangle$ ($10/9$ compared to $2/3$). Consequently, the saturated population is mainly determined by branching ratios.

We can calculate the expected rate as $b_{\text{th}} = (R_{1 \rightarrow 2}^{\text{sun}} + R_{2 \rightarrow 1}^{\text{sun}}) / P_{\text{sun}}$ using Eqs. (5) and (6). Using the experimental spectrum, we calculate the fraction $\kappa \approx 3.7 \times 10^{-8}$ of the Sun power at the atomic transition out of the total Sun power, leading to $R_0 / P_{\text{sun}} \approx 8.6\text{s}^{-1}\text{nW}^{-1}$ and a theoretical rate towards saturation $b_{\text{th}} = (16/9)R_0 / P_{\text{sun}} \approx 15\text{s}^{-1}\text{nW}^{-1}$, a 3σ difference relative to the observation. The discrepancy can be explained in part by the wavelength-dependence of the high-NA lens' focal length, which makes impossible optimal focusing of all the resonant light^{28,34}.

B. Detection of signal photons embedded in sunlight

For the rest of the experimental runs, the sunlight was mixed with laser photons tuned to the D_2 , $F = 1 \rightarrow F' = 2$ transition, and the probability to find the atom in $|2\rangle$ under this combined illumination was measured. Figure 3 shows

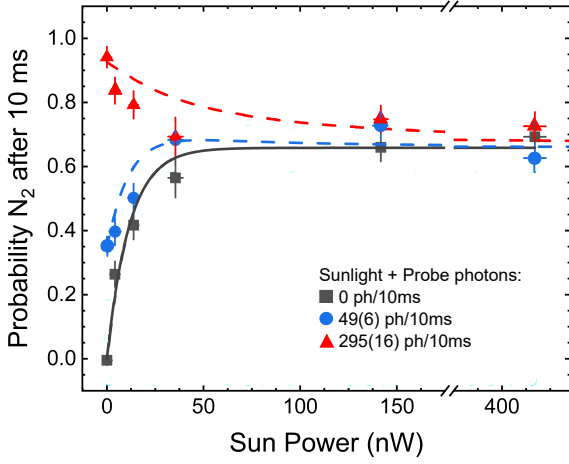


FIG. 3. Sunlight combined with probe saturation curves. Data points show the probability of the atom being in $|2\rangle$ after the exposure time of 10 ms and its uncertainty, for sunlight combined with probe photons at 0 ph/10ms (black), 49(6) ph/10ms (blue) and 295(16) ph/10ms (red). Solid grey lines show data fitted with Eq. (9) with parameters $N_2^{\text{sat,exp}} = 0.66(3)$, $b_{\text{exp}} = 9(2) \text{ nW}^{-1} \text{ s}^{-1}$. Dashed lines plot the theoretical expectation of Eq. (2) without any free parameters, where the rates were calculated using Eq. (7) with $N_2^{\text{sat,exp}}$ and b_{exp} from the fitted Sun data, $\eta_{\text{QJ}} = 8.5(5) \times 10^{-3}$ and corresponding probe photon numbers for low probe (blue) and high probe (red).

experimental points corresponding to sending laser signals of 49(6) ph/10ms (blue circles) and 295(16) ph/10ms (red triangles). Solid lines show the probability of the atom ending in $|2\rangle$ according to our model given the numbers of probe photons and the fitted Sun parameters $N_2^{\text{sat,exp}}$ and b_{exp} , showing a good agreement between experimental data and our model's expectations.

To give some context for these numbers, we consider an extreme background-rejection problem: a hypothetical space probe flies near to the surface of the Sun, while sending laser signals to an Earth-based telescope in the presence of full solar background, as in Figure 1a. Assuming typical apertures for satellite- and ground-based telescopes³⁷ of $A_T = 5 \times 10^{-4} \text{ m}^2$ and $A_R = 0.8 \text{ m}^2$ for the transmitter and receiver, respectively, and a link distance of about 1 AU (astronomical unit), the link efficiency is $\eta_{\text{link}} \approx 1 \times 10^{-14}$. If the probe emits a 1 W signal at $\lambda = 780 \text{ nm}$, the flux of the collected probe photons on Earth would be 400 photons/10ms. This is similar to our 295 probe photons case for which the signal is well distinguishable from the solar background.

We now calculate the signal-to-noise ratio (SNR) of the QJPD when detecting signal photons mixed with sunlight photons. It is defined using the quantum efficiency and number of sent signal photons, η_{sig} and N_{sig} , and the quantum efficiency and number of sunlight photons, η_{bg} and N_{bg}

$$\text{SNR} = \frac{N_{\text{sig}} \eta_{\text{sig}}}{N_{\text{bg}} \eta_{\text{bg}}}. \quad (10)$$

The QJPD has detection efficiency on the probe transition $\eta_{\text{sig}} = \eta_{\text{QJ}}$. It responds to sunlight photons within the 6 MHz transition linewidth including all transitions causing a jump from $|1\rangle$ to $|2\rangle$. From the total rate given by Eq. (5), we already calculated $R_{1 \rightarrow 2}^{\text{sun}} = (10/9)R_0$, from which the probe transition contribution is $(5/12)R_0$. As calculated in the previous section, the fraction of solar photons within the transition linewidth is given by $\kappa \approx 3.7 \times 10^{-8}$, leading to a sensitivity to background $\eta_{\text{bg}} = (8/3)\kappa\eta_{\text{QJ}}$. Taking the number of signal photons from the previous example, $N_{\text{sig}} = 400 \text{ ph/10ms}$, and the number of solar photons in 1 nW, $N_{\text{bg}} = 5 \times 10^7 \text{ ph/10ms}$, the SNR of the QJPD is 80.

For comparison, we consider a filtered detector consisting of a narrowband filter with transmission $T(\lambda)$, maximum transmission T_{max} , and bandwidth $\Delta\lambda$, used before a broadband detector with quantum efficiency η_{det} . In that case, the background sensitivity is $\eta_{\text{bg}} = \eta_{\text{det}} T_{\text{max}} \Delta\lambda B_{\text{exp}}(\lambda_0) / \int_0^\infty B_{\text{exp}}(\lambda) d\lambda = \kappa_{\text{filter}} T_{\text{max}} \eta_{\text{det}}$ for constant detector efficiency η_{det} across the solar spectrum, while the quantum efficiency for signal is simply $\eta_{\text{sig}} = T_{\text{max}} \eta_{\text{det}}$.

For example, FADOF filters for Rb have achieved “ultra-narrow” bandwidths (equivalent noise bandwidth or ENBW) down to 1 GHz^{38,39}, giving $\kappa_{\text{filter}} = 6 \times 10^{-6}$, with 70 % maximum transmission. Combining this filter with a detector (e.g., superconducting photon counters) with near-unit detection efficiency would achieve $\eta_{\text{bg}} = 4.2 \times 10^{-6}$ and $\eta_{\text{sig}} = 0.7$. Taking as above $N_{\text{sig}} = 400 \text{ ph/10ms}$ and $N_{\text{bg}} = 5 \times 10^7 \text{ ph/10ms}$ leads to an SNR equal to 1 for this filtered detector, almost two orders of magnitude below the performance of the QJPD detector.

C. Channel capacity

Let us consider a communication scenario where information is transmitted between a sender (bit $X = 0, 1$), for example a satellite, and a receiver on Earth (bit $Y = 0, 1$) in the presence of sunlight background. In information theory, the amount of received information over a classical noisy communication channel can be quantified using Shannon's channel capacity⁴⁰ that maximizes, over the input probability distribution $q = p(x = 1)$, the mutual information $I(X; Y)$ between the sent and received information

$$C = \max_q I(X; Y), \quad (11)$$

where the mutual information is

$$I(X; Y) = \sum_{x,y} p(x) p(y|x) \log_2 \frac{p(y|x)}{p(y)}. \quad (12)$$

We calculate Eq. (11) using the probability of detecting signal photons $p_s = p(y = 1|x = 1) = N_2$, and the probability of detecting background photons $p_b = p(y = 1|x = 0) = N_2^{\text{background}}$. Figure 4 shows the channel capacity. For instance, a channel capacity of 0.5 bits/use is obtained for 150 probe photons in 10 ms in 1 nW of sunlight, where error correction codes via redundancy can be applied for transmitting information⁴⁰. This motivates the use of an atomic photodetector for low-light detection in broadband background.

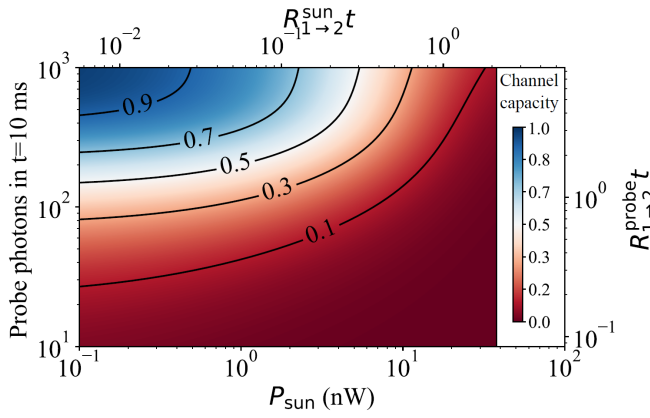


FIG. 4. Calculated channel capacity for a binary communication channel in presence of background photons for the atomic detector.

V. CONCLUSION

In conclusion, we have demonstrated the background rejection capabilities of using a single atom, in our case ^{87}Rb , as a photodetector. By measuring quantum jump rates, photon-level signals can be detected with high fidelity even when embedded in up to tens of nW of sunlight power. The atomic dynamics driving the quantum jump rates are modeled using Einstein rate equations to quantify transitions caused by resonant sunlight. The model is found to agree well with experimental data, and is used to further calculate a channel capacity for the detection of optical signals in the presence of sunlight background using a single atom as a photodetector. The AC Stark shift caused by off-resonant background photons is calculated and found to be on the order of a few hundreds of Hz per μW of Sun power. This does not significantly contribute to the internal population dynamics for rubidium atoms, but can be relevant for atoms with narrower lines.

We studied the extreme case where the background is given by sunlight. However, there are applications dealing with lower background levels, as given by skylight, whose radiance on clear days is a factor of 2000 lower in intensity than sunlight⁴¹, significantly increasing the channel capacity (Figure 4).

Frequency matching to the desired atomic transition is a requirement of this technique, which can be fulfilled both by tuning the emitter frequency or by tuning the light-shifts of the atom in the trap, for instance using the excited-to-excited state transition at 1529 nm for Rb atoms^{42,43} to compensate Doppler shifts caused by a relative motion between emitter and receiver^{44,45}.

While we have used the QJPD for detection of classical signals, we note that closely-related techniques have been used for quantum memory and can coherently store quantum information encoded in photon polarization⁴⁶.

The model for sunlight-atom interaction is general and can be applied to any atom by including the necessary transitions for calculating the rates and the energy shifts. In particular, our results for Rb can be directly applied for studying the internal dynamics of mesospheric sodium¹² which have similar

hyperfine structure with D-lines at 589 nm.

ACKNOWLEDGMENTS

Funded by the by the European Commission projects Field-SEER (ERC 101097313), OPMMEG (101099379) and QUANTIFY (101135931); Spanish Ministry of Science MCIN project SALVIA (PID2024-158479NB-I00), “NextGenerationEU/PRTR.” (Grant FJC2021-047840-I) and “Severo Ochoa” Center of Excellence CEX2024-001490-S [MICIU/AEI/10.13039/501100011033]; Generalitat de Catalunya through the CERCA program, DURSI grant No. 2021 SGR 01453 and QSENSE (GOV/51/2022). Fundació Privada Cellex; Fundació Mir-Puig. LZ acknowledges the “Presidencia de la Agencia Estatal de Investigación” grant Ref. PRE2020-094392. TL acknowledges Marie Skłodowska-Curie grant agreement No 847517. Views and opinions expressed are those of the authors only and do not necessarily reflect those of the European Union or the European Research Council Executive Agency. Neither the European Union nor the granting authority can be held responsible for them.

DATA AVAILABILITY STATEMENT

The data that support the findings of this study are available from the corresponding author upon reasonable request.

AUTHOR DECLARATIONS

Conflict of interest

The authors have no conflicts to disclose.

Author Contributions

L. Zarraoa: Formal Analysis (equal), Investigation (equal), Methodology (equal), Conceptualization (equal), Writing-Original draft Preparation (equal), Writing-Review and Editing (equal). **R. Veyron:** Formal Analysis (equal), Investigation (equal), Methodology (equal), Conceptualization (equal), Supervision (equal), Writing-Original draft Preparation (equal), Writing-Review and Editing (equal). **T. Lamich:** Writing-Original draft Preparation (supporting), Writing-Review and Editing (equal). **S. Elsehmy:** Writing-Original draft Preparation (supporting), Writing-Review and Editing (equal). **M.W. Mitchell:** Funding Acquisition (lead), Supervision (equal), Conceptualization (equal), Methodology (equal), Writing-Original draft Preparation (equal), Writing-Review and Editing (equal).

REFERENCES

- ¹S.-K. Liao, H.-L. Yong, C. Liu, G.-L. Shentu, D.-D. Li, J. Lin, H. Dai, S.-Q. Zhao, B. Li, J.-Y. Guan, W. Chen, Y.-H. Gong, Y. Li, Z.-H. Lin, G.-S. Pan, J. S. Pelc, M. M. Fejer, W.-Z. Zhang, W.-Y. Liu, J. Yin, J.-G. Ren, X.-B. Wang, Q. Zhang, C.-Z. Peng, and J.-W. Pan, "Long-distance free-space quantum key distribution in daylight towards inter-satellite communication," *Nature Photonics* **11**, 509–513 (2017).
- ²M. Avesani, L. Calderaro, M. Schiavon, A. Stanco, C. Agnesi, A. Santamato, M. Zahidy, A. Scriminich, G. Foletto, G. Contestabile, M. Chiesa, D. Rotta, M. Artiglia, A. Montanaro, M. Romagnoli, V. Sorianello, F. Vedovato, G. Vallone, and P. Villoresi, "Full daylight quantum-key-distribution at 1550 nm enabled by integrated silicon photonics," *npj Quantum Information* **7** (2021), 10.1038/s41534-021-00421-2.
- ³W.-Q. Cai, Y. Li, B. Li, J.-G. Ren, S.-K. Liao, Y. Cao, L. Zhang, M. Yang, J.-C. Wu, Y.-H. Li, W.-Y. Liu, J. Yin, C.-Z. Wang, W.-B. Luo, B. Jin, C.-L. Lv, H. Li, L. You, R. Shu, G.-S. Pan, Q. Zhang, N.-L. Liu, X.-B. Wang, J.-Y. Wang, C.-Z. Peng, and J.-W. Pan, "Free-space quantum key distribution during daylight and at night," *Optica* **11**, 647 (2024).
- ⁴L. Du, J. Wang, Y. Yang, Y. Xun, F. Li, F. Wu, S. Gong, H. Zheng, X. Cheng, G. Yang, and Z. Lu, "Continuous detection of diurnal sodium fluorescent lidar over beijing in china," *Atmosphere* **11** (2020), 10.3390/atmos11010118.
- ⁵M. Hart, S. M. Jefferies, and N. Murphy, "Daylight operation of a sodium laser guide star for adaptive optics wavefront sensing," *Journal of Astronomical Telescopes, Instruments, and Systems* **2**, 040501–040501 (2016).
- ⁶A. Ntanos, A. Stathis, P. Kourelas, E. Kyriazi, P. Toumasis, N. K. Lyras, N. Makris, S. Tsavdaridis, E. M. Xilouris, A. Marousis, I. Papastamatiou, A. D. Panagopoulos, K. Vyrsoinos, K. Tsiganis, G. T. Kanellos, H. Avramopoulos, and G. Giannoulis, "SMF Coupled Compact Ground Terminal with Advanced Filtering Towards Daylight C Band Satellite QKD," (2025), 10.48550/arXiv.2509.07667.
- ⁷J. A. Zielińska, F. A. Beduini, N. Godbout, and M. W. Mitchell, "Ultra-narrow Faraday rotation filter at the Rb D₁ line," *Opt. Lett.* **37**, 524–526 (2012).
- ⁸J. A. Zielińska, F. A. Beduini, V. G. Lucivero, and M. W. Mitchell, "Atomic filtering for hybrid continuous-variable/discrete-variable quantum optics," *Opt. Express* **22**, 25307–25317 (2014).
- ⁹Y. Liu, X. Dong, J. Gao, B. Guan, Y. Zheng, Z. Liang, X. Han, and H. Dong, "Real-Time Identification Algorithm of Daylight Space Debris Laser Ranging Data Based on Observation Data Distribution Model," *Sensors (Basel, Switzerland)* **25**, 7 (2025), 10.3390/s25072281.
- ¹⁰Y. Xia, X. Cheng, Z. Wang, L. Liu, Y. Yang, L. Du, J. Jiao, J. Wang, H. Zheng, Y. Li, F. Li, and G. Yang, "Design of a data acquisition, correction and retrieval of Na Doppler lidar for diurnal measurement of temperature and wind in the mesosphere and lower thermosphere region," *Remote Sensing* **15** (2023), 10.3390/rs15215140.
- ¹¹C. C. Evans, D. N. Woolf, J. M. Brown, and J. M. Hensley, "A daytime free-space quantum-optical link using atomic-vapor spectral filters," in *2019 Conference on Lasers and Electro-Optics (CLEO)* (2019) pp. 1–2.
- ¹²J. M. Higbie, S. M. Rochester, B. Patton, R. Holzlöhner, D. Bonaccini Calia, and D. Budker, "Magnetometry with mesospheric sodium," *Proceedings of the National Academy of Sciences* **108**, 3522–3525 (2011).
- ¹³T. J. Kane, P. D. Hillman, C. A. Denman, M. Hart, R. Phillip Scott, M. E. Purucker, and S. J. Potashnik, "Laser remote magnetometry using mesospheric sodium," *Journal of Geophysical Research: Space Physics* **123**, 6171–6188 (2018).
- ¹⁴F. Pedreros Bustos, D. Bonaccini Calia, D. Budker, M. Centrone, J. Hellemeier, P. Hickson, R. Holzlöhner, and S. Rochester, "Remote sensing of geomagnetic fields and atomic collisions in the mesosphere," *Nature Communications* **9** (2018), 10.1038/s41467-018-06396-7.
- ¹⁵A. M. Akulshin, D. Budker, F. Pedreros Bustos, T. Dang, E. Klinger, S. M. Rochester, A. Wickenbrock, and R. Zhang, "Remote detection optical magnetometry," *Physics Reports* **1106**, 1–32 (2025), remote Detection Optical Magnetometry.
- ¹⁶L. Spogli, L. Alfonsi, and C. Cesaroni, "Stepping into an equatorial plasma bubble with a swarm overfly," *Space Weather* **21**, e2022SW003331 (2023), e2022SW003331 2022SW003331, <https://agupubs.onlinelibrary.wiley.com/doi/pdf/10.1029/2022SW003331>.
- ¹⁷K. Beloy, U. I. Safronova, and A. Derevianko, "High-accuracy calculation of the blackbody radiation shift in the ¹³³Cs primary frequency standard," *Phys. Rev. Lett.* **97**, 040801 (2006).
- ¹⁸Y. S. Hassan, K. Beloy, J. L. Siegel, T. Kobayashi, E. Swiler, T. Grogan, R. C. Brown, T. Rojo, T. Bothwell, B. D. Hunt, A. Halaoui, and A. D. Ludlow, "Cryogenic optical lattice clock with 1.7×10^{-20} blackbody radiation stark uncertainty," *Physical Review Letters* **135** (2025), 10.1103/4tky-jmsm.
- ¹⁹T. F. Gallagher and W. E. Cooke, "Interactions of blackbody radiation with atoms," *Physical Review Letters* **42**, 835–839 (1979).
- ²⁰J. W. Farley and W. H. Wing, "Accurate calculation of dynamic stark shifts and depopulation rates of rydberg energy levels induced by blackbody radiation. hydrogen, helium, and alkali-metal atoms," *Phys. Rev. A* **23**, 2397–2424 (1981).
- ²¹I. I. Beterov, I. I. Ryabtsev, D. B. Tretyakov, and V. M. Entin, "Quasiclassical calculations of blackbody-radiation-induced depopulation rates and effective lifetimes of rydberg *ns*, *np*, and *nd* alkali-metal atoms with $n \leq 80$," *Phys. Rev. A* **79**, 052504 (2009).
- ²²S. Hoekstra, J. J. Giljames, B. Sartakov, N. Vanhaecke, L. Scharfenberg, S. Y. T. van de Meerakker, and G. Meijer, "Optical pumping of trapped neutral molecules by blackbody radiation," *Phys. Rev. Lett.* **98**, 133001 (2007).
- ²³M. Sonnleitner, M. Ritsch-Marte, and H. Ritsch, "Attractive optical forces from blackbody radiation," *Phys. Rev. Lett.* **111**, 023601 (2013).
- ²⁴P. Haslinger, M. Jaffe, V. Xu, O. Schwartz, M. Sonnleitner, M. Ritsch-Marte, H. Ritsch, and H. Müller, "Attractive force on atoms due to blackbody radiation," *Nature Physics* **14**, 257260 (2018).
- ²⁵B. Décamps, A. Gauguet, J. Vigué, and M. Büchner, "Decoherence of a matter wave by blackbody radiation," *Physical Review A* **109** (2024), 10.1103/physreva.109.053306.
- ²⁶A. Younes and W. C. Campbell, "Laser-type cooling with unfiltered sunlight," *Phys. Rev. E* **109**, 034109 (2024).
- ²⁷A. Younes, R. Putnam, P. Hamilton, and W. C. Campbell, "Internal state cooling of an atom with thermal light," *Entropy* **27** (2025), 10.3390/e27030222.
- ²⁸L. Zarraoa, R. Veyron, T. Lamich, L. C. Bianchet, and M. W. Mitchell, "Quantum jump photodetector for narrowband photon counting with a single atom," *Phys. Rev. Res.* **6**, 033338 (2024).
- ²⁹N. Bruno, L. C. Bianchet, V. Prakash, N. Li, N. Alves, and M. W. Mitchell, "Maltese cross coupling to individual cold atoms in free space," *Opt. Express* **27**, 31042–31052 (2019).
- ³⁰L. C. Bianchet, N. Alves, L. Zarraoa, N. Bruno, and M. W. Mitchell, "Manipulating and measuring single atoms in the Maltese cross geometry," *Open Research Europe* **1**, 102 (2021).
- ³¹M. Iqbal, "Chapter 3 - the solar constant and its spectral distribution," in *An Introduction to Solar Radiation*, edited by M. Iqbal (Academic Press, 1983) pp. 43–58.
- ³²L. Wald, "BASICS IN SOLAR RADIATION AT EARTH SURFACE," (2018), working paper or preprint.
- ³³D. H. Sliski, C. H. Blake, J. D. Eastman, and S. Halverson, "Seeing the limited coupling of starlight into single-mode fiber with a small telescope," *Astronomische Nachrichten* **344**, e20220080 (2023), <https://onlinelibrary.wiley.com/doi/pdf/10.1002/asna.20220080>.
- ³⁴M. K. Tey, G. Maslennikov, T. C. H. Liew, S. A. Aljunid, F. Huber, B. Chng, Z. Chen, V. Scarani, and C. Kurtsiefer, "Interfacing light and single atoms with a lens," *New Journal of Physics* **11**, 043011 (2009).
- ³⁵C. Degenhardt, H. Stoeck, C. Lisdar, G. Wilpers, H. Schnatz, B. Lipphardt, T. Nazarova, P.-E. Pottie, U. Sterr, J. Helmcke, and F. Riehle, "Calcium optical frequency standard with ultracold atoms: Approaching 10^{-15} relative uncertainty," *Physical Review A* **72** (2005), 10.1103/physreva.72.062111.
- ³⁶B. Arora, M. S. Safronova, and C. W. Clark, "Magic wavelengths for the *np* – *ns* transitions in alkali-metal atoms," *Physical Review A* **76** (2007), 10.1103/physreva.76.052509.
- ³⁷D. Gigenbach, M. T. Knopp, and C. Fuchs, "Link budget calculation in optical leo satellite downlinks with on/off-keying and large signal divergence: A simplified methodology," *International Journal of Satellite Communications and Networking* **41**, 460–476 (2023), <https://onlinelibrary.wiley.com/doi/pdf/10.1002/sat.1478>.
- ³⁸J. A. Zielińska, F. A. Beduini, N. Godbout, and M. W. Mitchell, "Ultra-narrow faraday rotation filter at the rb d1 line," *Opt. Lett.* **37**, 524–526 (2012).

- ³⁹X. Liang, Y. Bai, L. Chen, X. Zhu, W. Zhou, L. Zhou, Q. Fu, Q. Zhou, X. Zou, W. Tan, X. Huang, L. Yin, and X. Fu, "Accurate measurement for the orbital angular momentum spectrum in scattering media based on a faraday atomic filter," *Opt. Lett.* **50**, 4162–4165 (2025).
- ⁴⁰C. E. Shannon, "A mathematical theory of communication," *Bell System Technical Journal* **27**, 379–423 (1948), <https://onlinelibrary.wiley.com/doi/pdf/10.1002/j.1538-7305.1948.tb01338.x>.
- ⁴¹C. Abbot, F. Fowle, and L. Aldrich, "The brightness of the sky," *Annals of the Astrophysical Observatory of the Smithsonian Institution* **3**, 141 (1932).
- ⁴²S. Coop, S. Palacios, P. Gomez, Y. N. M. de Escobar, T. Vanderbruggen, and M. W. Mitchell, "Floquet theory for atomic light-shift engineering with near-resonant polychromatic fields," *Optics Express*, *Optics Express* **25**, 32550–32559 (2017).
- ⁴³R. Veyron, J.-B. Gerent, G. Baclet, V. Mancois, P. Bouyer, and S. Bernon, "In situ subwavelength microscopy of ultracold atoms using dressed excited states," *PRX Quantum* **5**, 030349 (2024).
- ⁴⁴N. Ren, B. Zhao, B. Liu, and K. Hua, "Adaptive doppler compensation method for coherent lidar based on optical phase-locked loop," *Measurement* **187**, 110313 (2022).
- ⁴⁵S. M. McSorley, B. P. Dix-Matthews, A. M. Frost, A. S. McCann, S. F. Karpathakis, D. R. Gozzard, S. M. Walsh, and S. W. Schediwy, "Free-space optical-frequency comparison over rapidly moving links," *Phys. Rev. Appl.* **23**, L021003 (2025).
- ⁴⁶H. P. Specht, C. Nolleke, A. Reiserer, M. Uphoff, E. Figueroa, S. Ritter, and G. Rempe, "A single-atom quantum memory," *Nature* **473**, 190–193 (2011).
- ⁴⁷A. Holevo, "Quantum channel capacities," *Quantum Electronics* **50**, 440 (2020).
- ⁴⁸S. Shaklan and F. Roddier, "Coupling starlight into single-mode fiber optics," *Appl. Opt.* **27**, 2334–2338 (1988).
- ⁴⁹P. K. Tan, G. H. Yeo, H. S. Poh, A. H. Chan, and C. Kurtsiefer, "Measuring temporal photon bunching in blackbody radiation," *The Astrophysical Journal Letters* **789**, L10 (2014).
- ⁵⁰Y. Jiang, B. Liu, R. Wang, Z. Li, Z. Chen, B. Zhao, G. Guo, W. Fan, F. Huang, and Y. Yang, "Photon counting lidar working in daylight," *Optics and Laser Technology* **163**, 109374 (2023).
- ⁵¹J. A. Gelbwachs, "422.7-nm atomic filter with superior solar background rejection," *Opt. Lett.* **15**, 236–238 (1990).
- ⁵²Y. Xing, D. Xu, Y. Li, W. Zhang, and L. Chen, "Sunlight-Excited Spontaneous Parametric Down-Conversion for Quantum Imaging," (2025), [arXiv:2508.11207](https://arxiv.org/abs/2508.11207) [quant-ph].
- ⁵³F. Luo, Z. Yang, H. Zhao, L. Jiang, J. Sun, Q. Liu, R. Wang, W. Yang, H. Wang, and X. Xu, "Demonstration of a low-pressure rb amplifier with an fadof-coupled ultra-narrowed diode pumping source," *Opt. Express* **33**, 28832–28840 (2025).